Supplementary Information

Integrating Molecular Photoswitch Memory with Nanoscale Optoelectronics for Neuromorphic Computing

David Alcer[*1], Nelia Zaiats[*1], Thomas Kjellberg Jensen[*1], Abbey M. Philip[2], Evripidis Gkanias[3], Nils Ceberg[4], Abhijit Das[1], Stanley Heinze[4], Magnus Borgström[1], Barbara Webb[3], Bo W. Laursen[2], and Anders Mikkelsen[1]

[*]these authors contributed equally
[1]Department of Physics and NanoLund, Lund University, Sweeden
[2]Nano-Science Center and Department of Chemistry, University of Copenhagen, Universitetsparken 5, 2100 Copenhagen, Denmark
[3]School of Informatics, University of Edinburgh, 10 Crichton St, EH8 9AB, Edinburgh, UK
[4]Department of Biology, Lund University, Sweeden

Note: in the following, "DASA photoswitch", "DASA", "molecular dye", and variants thereof, are used interchangeably. In relation to experimental results, this refers to the specific DASA photoswitch molecule described in the Main Text and in the SI "Synthesis" section.

Supplementary Information Table of Contents

Supplementary Text S1. Model of the DASA molecular photoswitch. The DASA transmittance is the fraction of light passing through the sample. This can be defined as a function of the absorbent (ON-state) molecules as per the Beer-Lambert Law,

$$T_i(t) = 10^{-A_i(t)}. \tag{1}$$

The absorbance (A) can be calculated as

$$A_i(t) = \epsilon\, l\, (c_{\text{tot}} – c_i(t)), \tag{2}$$

where ϵ is the molar absorption coefficient, l is the optical path length through the sample (thickness of the DASA layer), and c_{tot} is the total concentration ($c_{\text{tot}} = c + c^{\text{ON}}$). Finally, the concentration of the OFF-state molecules (c) can be approximated by the below differential equation,

$$c_i(t) = (1 - k\,\mathrm{d}t)\, c_i(t - \mathrm{d}t) + k_\phi\, \phi\, I_i(t)\, (1 - T_i(t - \mathrm{d}t))\, \mathrm{d}t. \tag{3}$$

Here, k is the rate coefficient that controls the (first order) back-reaction (related to the half-life as $k = \log 2 \,/\, T_{\frac{1}{2}}$), I_i is the incident light, and ϕ is the proportion of the absorbed light that leads to switching. Note that ϕ represents a probability (known as the quantum yield) that the molecule will switch to its metastable photo stationary state (OFF state). In equation (3), k_ϕ is calculated as

$$k_\phi = \frac{W_{\max}}{E\, V\, N_A}, \qquad\qquad E = \frac{h\, c}{\lambda} \tag{4}$$

where $W_{\max}$ is the optical effect, V is the volume of the material, $N_A = 6.022\,140\,76 \times 10^{23}\,\text{mol}^{-1}$ is the Avogadro's constant, $h = 6.625\,979\,15 \times 10^{-34}\,\text{J}\,\text{sec}$ is the Plank's constant, $c = 299\,792\,458\,\text{m}\,\text{sec}^{-1}$ is the speed of light, and λ is the wavelength of the incident light.

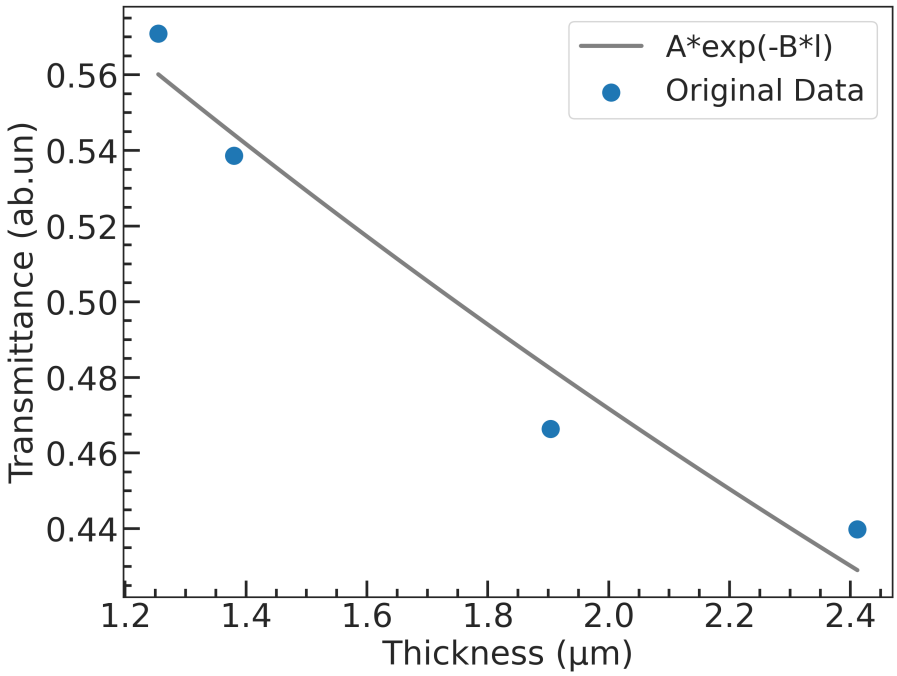

Supplementary Figure S1 Transmittance of DASA thin films on Al_2O_3

This Figure shows the measured transmittance of DASA/PAMS (poly(α-methyl)styrene) thin films on sapphire, as a function of the film thickness. The data is described by a decaying exponential function (A = 0.7480, B = 0.2305), in accordance with the Beer-Lambert law.

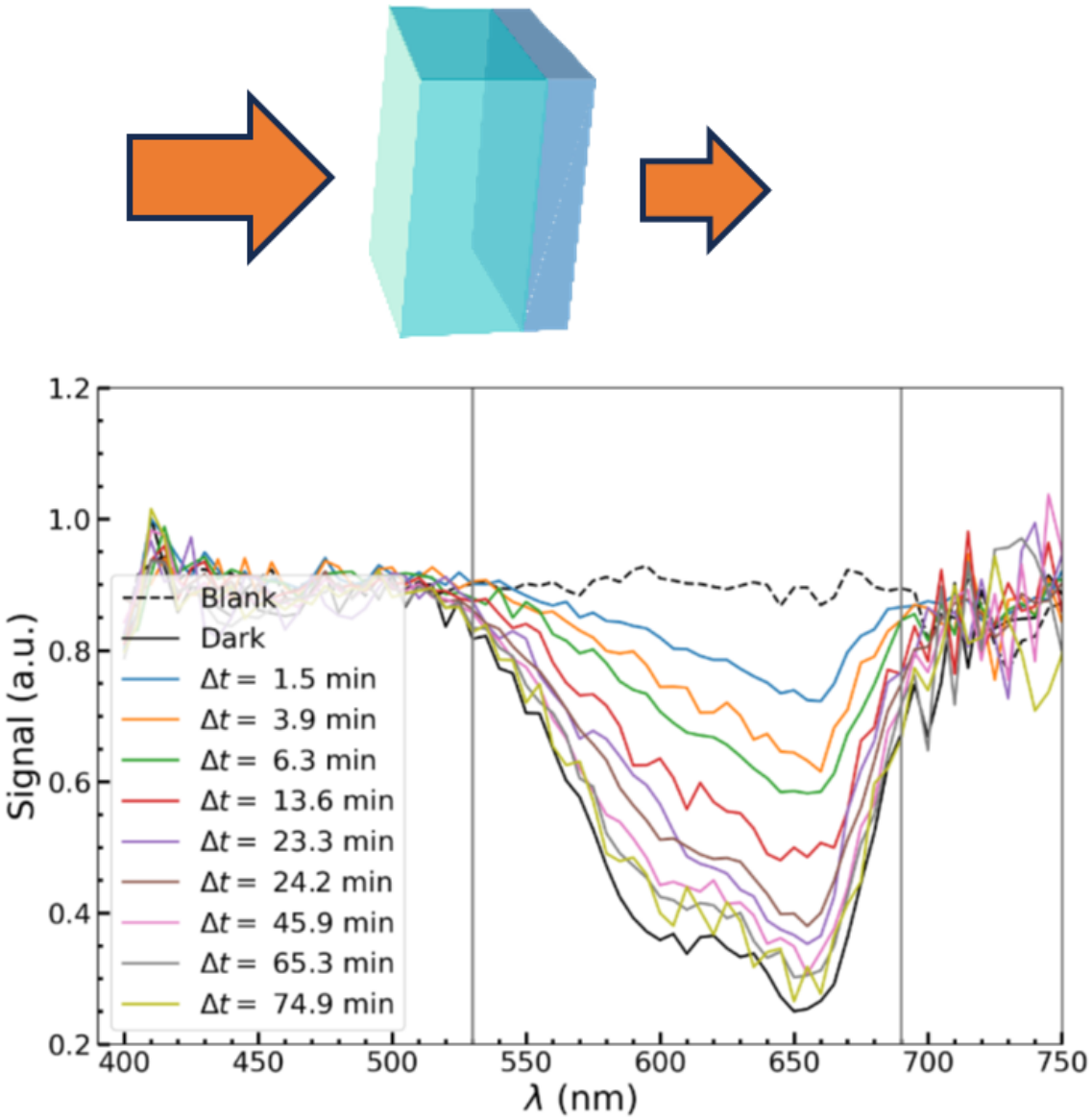

Supplementary Figure S2 Transmission spectrum of a PAMS film with DASA as a function of time spent in the dark after high-intensity illumination.

The Figure illustrates the recovery of absorption of a DASA/PAMS film over time after bleaching. The transmission spectra were recorded using the integrating sphere of a Bentham PVE3000 system (see main text), and are normalized to the signal when no sample is present. The dashed line ("Blank") shows the transmission of a blank piece of sapphire. The full, black line ("Dark") shows the transmission spectrum of the sample after a DASA/PAMS film has been deposited on the sapphire piece by drop casting, but before it has been exposed to high-intensity illumination. In this situation, only a very small fraction of the DASA molecules are in the bleached state and the transmission is minimal. The sample was then exposed high-intensity illumination for 15 minutes, in order to achieve a large degree of bleaching. The colored lines show how the transmission spectrum of the sample evolves over time after bleaching. The times noted in the legend are counted from when the high-intensity illumination was turned off. After 75 minutes, the DASA layer transmission is within a few percent of the original "Dark" curve.

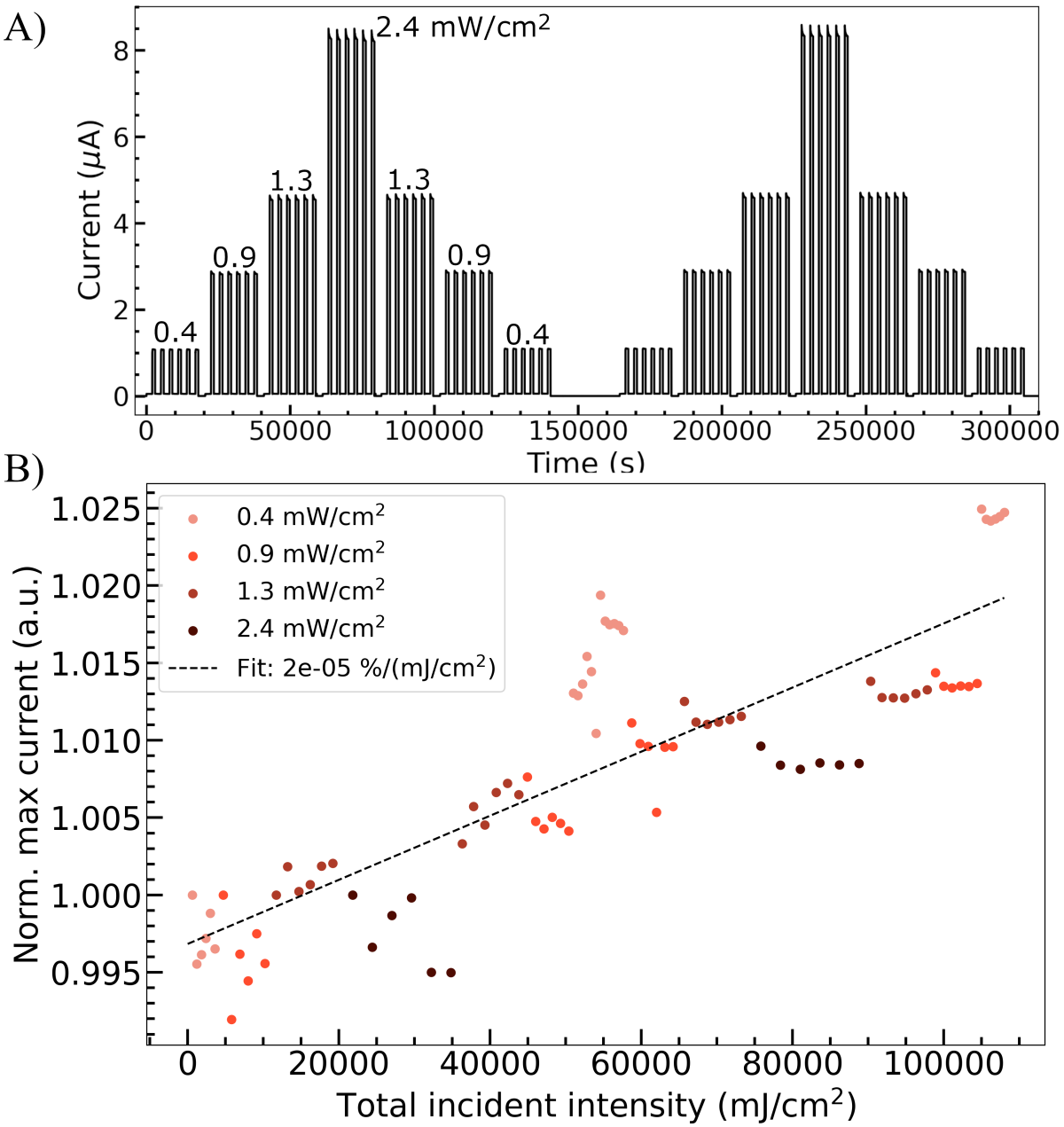

Supplementary Figure S3 Evaluation of permanent photobleaching after long-duration high intensity illumination.

A) Shows an overview of a measurement where an nanowire array covered with DASA was illuminated at high intensities for long durations. The measurement consists of a doublet of seven illumination sets. Each illumination set consists of 6×1000 s high-intensity illumination periods at constant intensity I_{high}, where I_{high} is 0.4, 0.9, 1.3 or 2.4 mW/cm^2, as denoted in the Figure. The high-intensity periods are separated by low-intensity periods, totalling 6×2000 s at $I_{low} = 0.1$ mW/cm^2 per set. The light is turned off for 2400 s in-between each set, and for 24 000 s at the midpoint of the measurement. **B)** Shows the maximum photocurrent attained for each high-intensity period, normalized to the first photocurrent maximum value of each I_{high} intensity. The x-axis shows the time-integrated light intensity incident on the sample. As would be expected from permanent photobleaching, a linear trend of increasing photocurrent is observed, at a rate of approximately $+2 \times 10^{-5}$% per mJ/cm^2. As some of the increased transmittance could be due to reversible bleaching, which would recover over time, these results constitute an upper bound to the effect of permanent photobleaching.

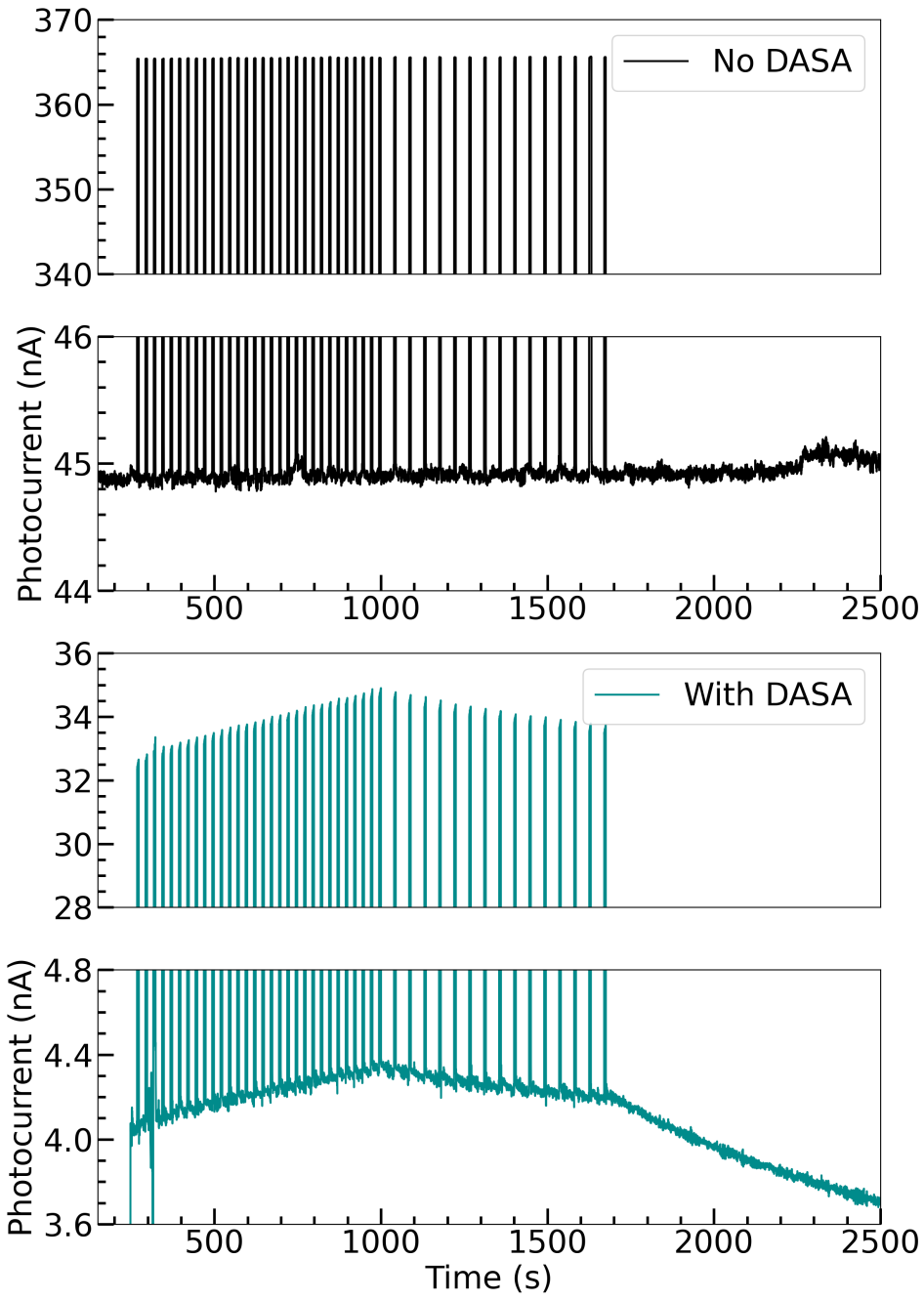

Supplementary Figure S4. Measurements using pulsed light signals to illustrate STP Top is the measurement on a nanowire array with no DASA, and no memory effect is seen. Bottom is the measurement of the current seen in the nanowire array with a DASA on top and a clear memory effect is seen. The low and high intensity of light can be used for read and write respectively (high also gives a measurement of DASA transparency). This measurement is identical to the one presented in main text Figure 4A, with the difference that the DASA/PAMS layer has been changed where a faster memory decay (back-reaction) is found. As a result, a the initial fast rate of spikes will still lead to an increased decolourisation (hence the increase in transmission), while the slower spike rate set in after a third of the experimental time no longer leads to an increased decolourisation, but instead gives a decrease. This difference between Fig S4 and Fig 4a illustrates STP behaviors as the dye memory decay time is changed.

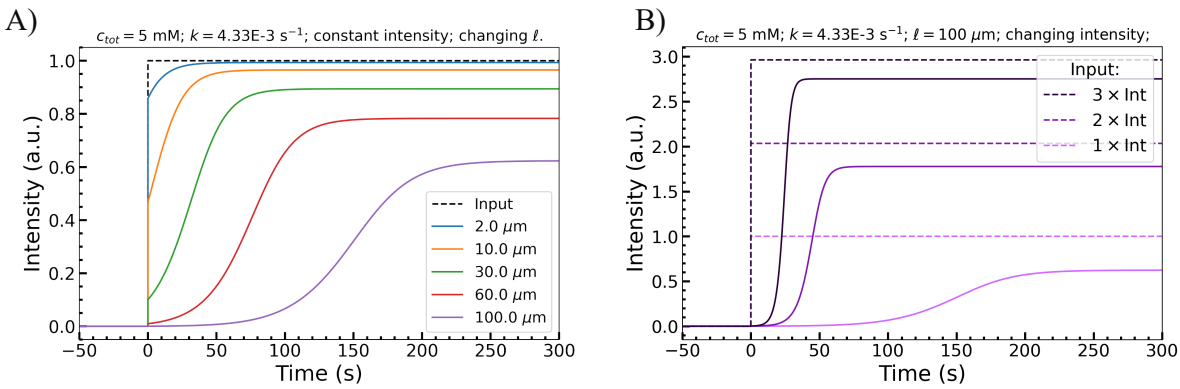

Supplementary Figure S5. Example simulations using the Beer-Lambert DASA model.

By numerically solving the differential equation Eq. 3, it is possible to show qualitatively how DASA layer thickness and the intensity of the illuminating light affect the dynamics of the DASA photoswitch. In these simulations, the total DASA concentration c_{tot} and the back-reaction rate k are kept constant. **A)** The illuminating light is turned on at Time = 0 s (dashed line "Input") and kept at a constant intensity. The solid lines show the light transmitted through the DASA film for a variety of DASA layer thicknesses ℓ (see legend). The same light intensity is used for all values of ℓ. During constant illumination, the DASA is gradually bleached, leading to an increase of transmitted light as a function of time. For the thicker films, the bleaching follows a sigmoidal time-evolution, while the bleaching of the thinner films are well-described by a single exponential. **B)** Here, ℓ is kept constant at 100 μm and the light intensity varied. Again, the dashed lines show the input light intensity, and the solid curves the transmitted light. At low intensity, the light-transmission as a function of time retains its sigmoidal shape, but for higher input intensities this shape becomes less pronounced, as the bleaching occurs much faster and reaches a higher maximum transmitted intensity.

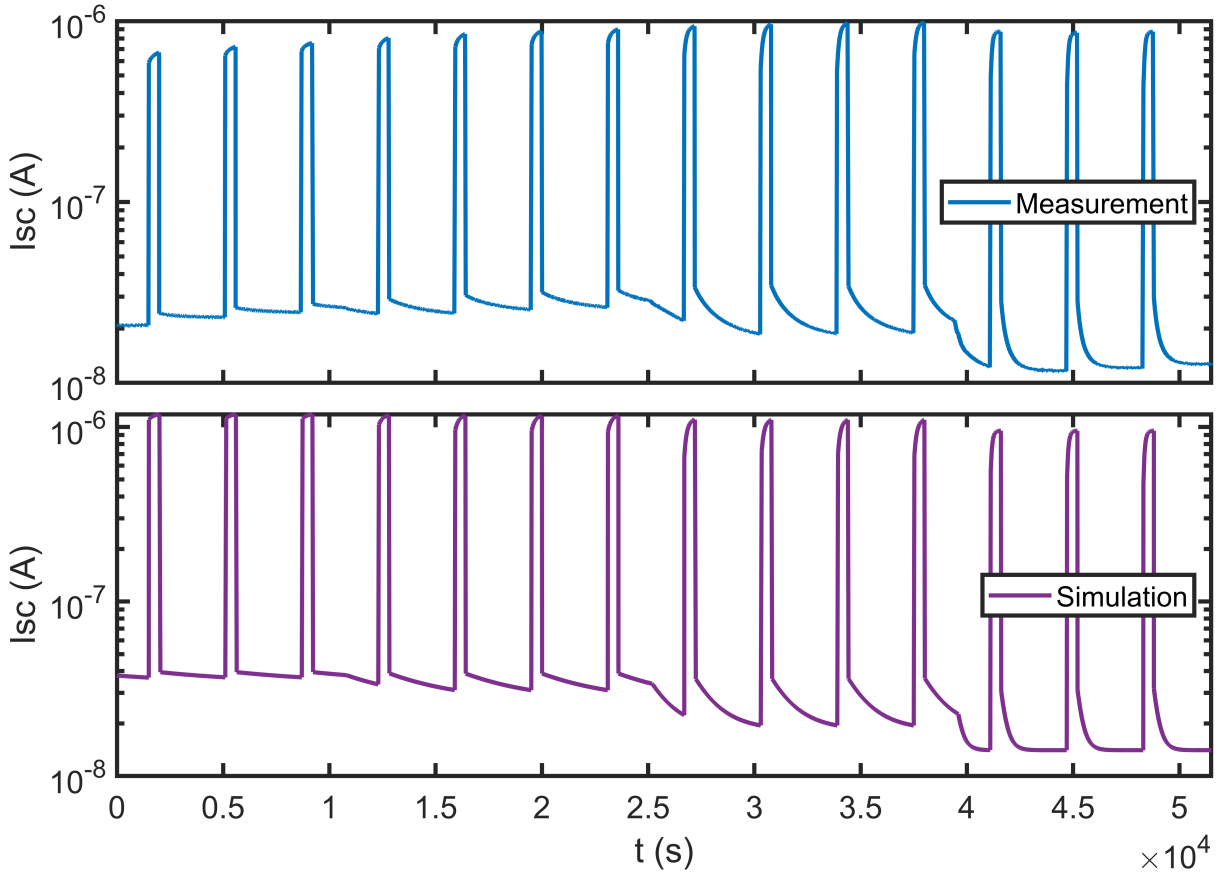

Supplementary Figure S6 Measurement data of the temperature dependent measurement together with a simulated result based on the DASA recovery rate derived from an activation energy barrier of 1.25 eV.

The Figure shows the measured (upper panel) and simulated (lower panel) photocurrent generated by an InP nanowire array solar cell device, covered in a thin film of DASA/PAMS. The temperature was switched between 21 °C, 28 °C, 38 °C and 48 °C at the times 1.05×10^4 s, 2.5×10^4 s, and 3.95×10^4 s, respectively. The illumination intensity was switched between the write intensity of 0.35 mW/cm^2 and the read intensity of 2.2 $\times 10^{-}3$ mW/cm^2.

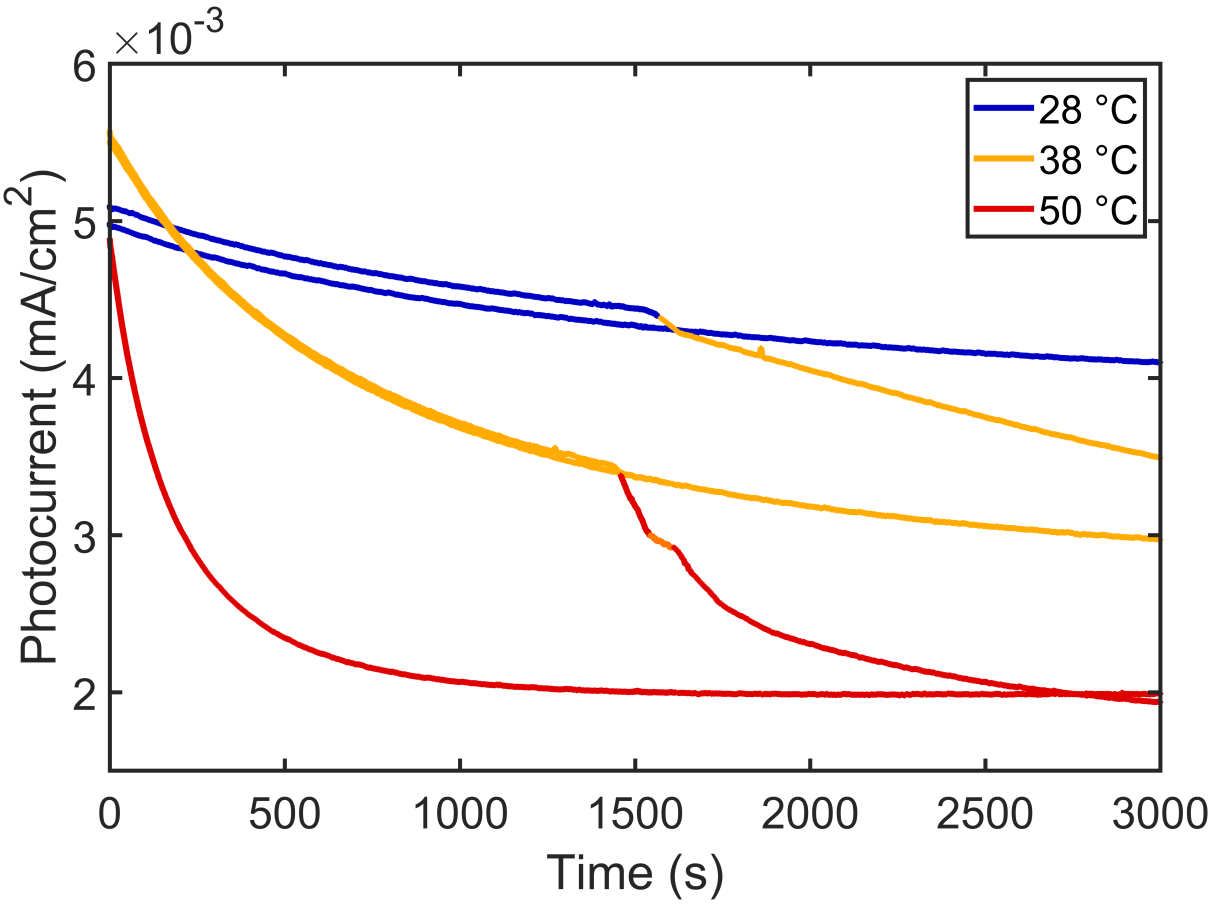

Supplementary Figure S7 DASA recovery at different temperatures in thin film

The Figure shows the measured photocurrent generated by an InP nanowire array solar cell device, covered in a thin film of DASA/PAMS. Each curve was measured at the indicated temperature at the read intensity of 2.2 $\times 10^{-}3$ mW/cm^2 after being exposed to the write intensity of 0.35 mW/cm^2. The data is derived from the measurement in SI Fig. 5.

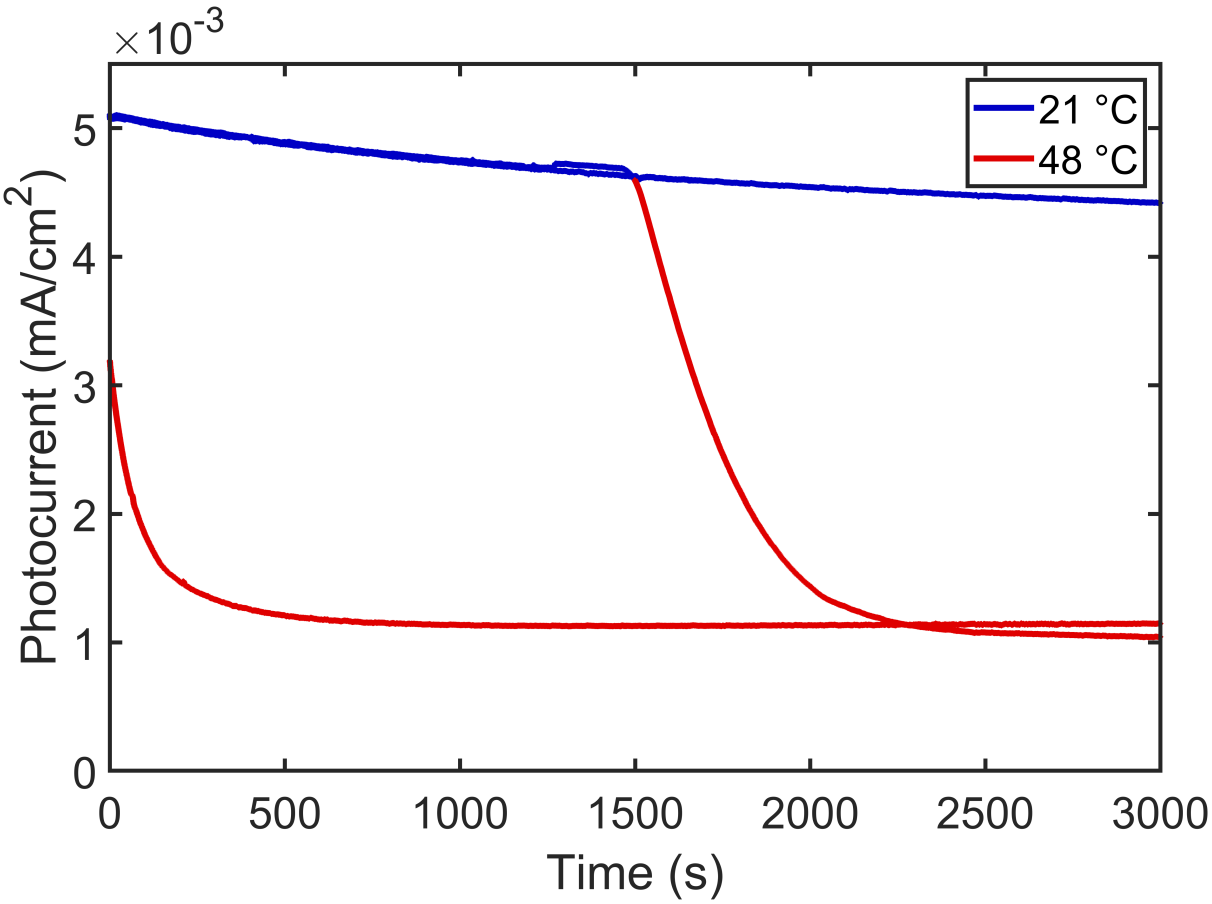

Supplementary Figure S8 Heating reset of the DASA memory

The Figure shows the measured photocurrent generated by an InP nanowire array solar cell device, covered in a thin film of DASA/PAMS. Each curve was measured at the indicated temperature at the read intensity of 2.2 $\times 10^{-}3$ mW/cm^2 after being exposed to the write intensity of 0.35 mW/cm^2.

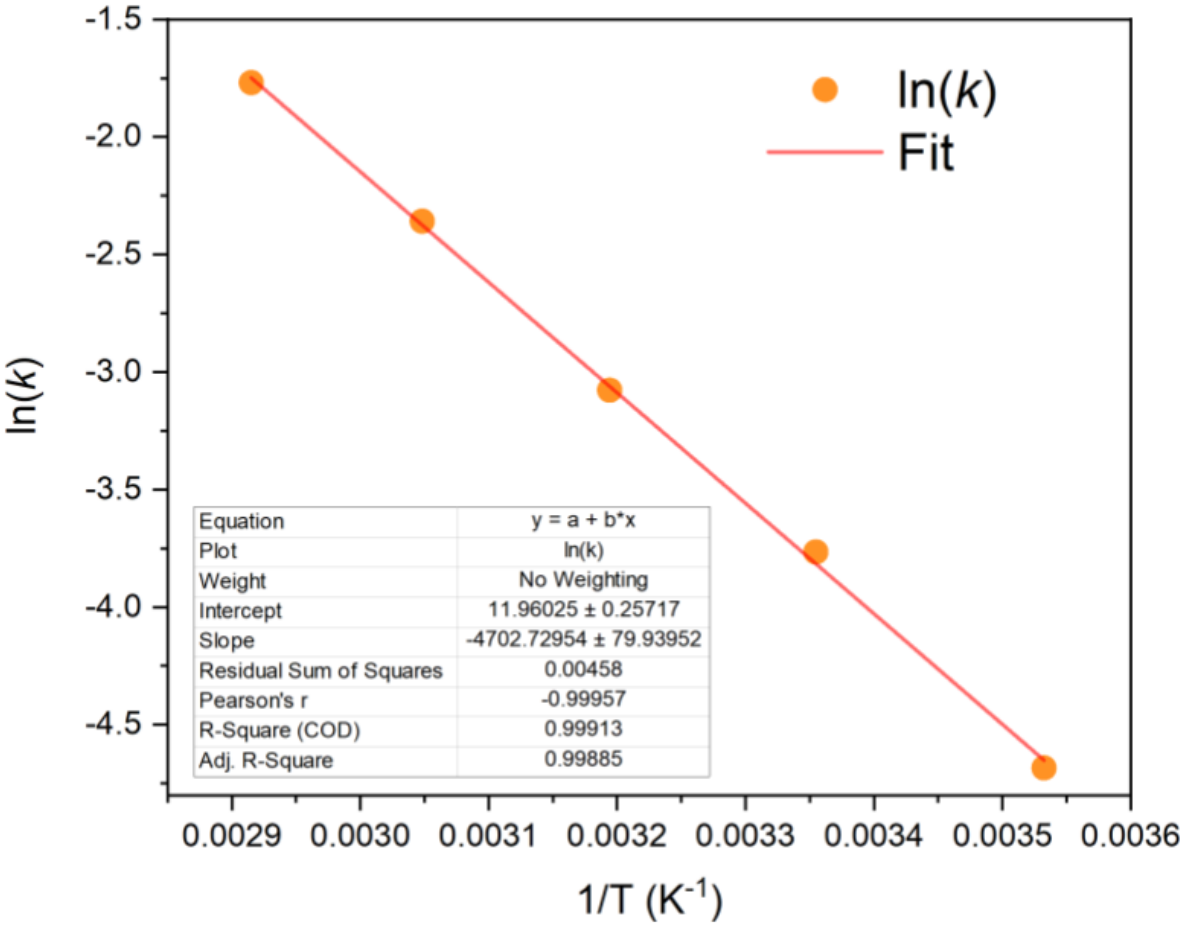

Supplementary Figure S9 Recovery rate of the DASA in toluene as a function of temperature in an Arrhenius plot

The activation energy for the thermally activated back reaction of the DASA in toluene solution is found to be 39 kJ/mol. This is to be compared to the activation energy in PAMS thin film, found to be 120 kJ/mol (see Main Text).

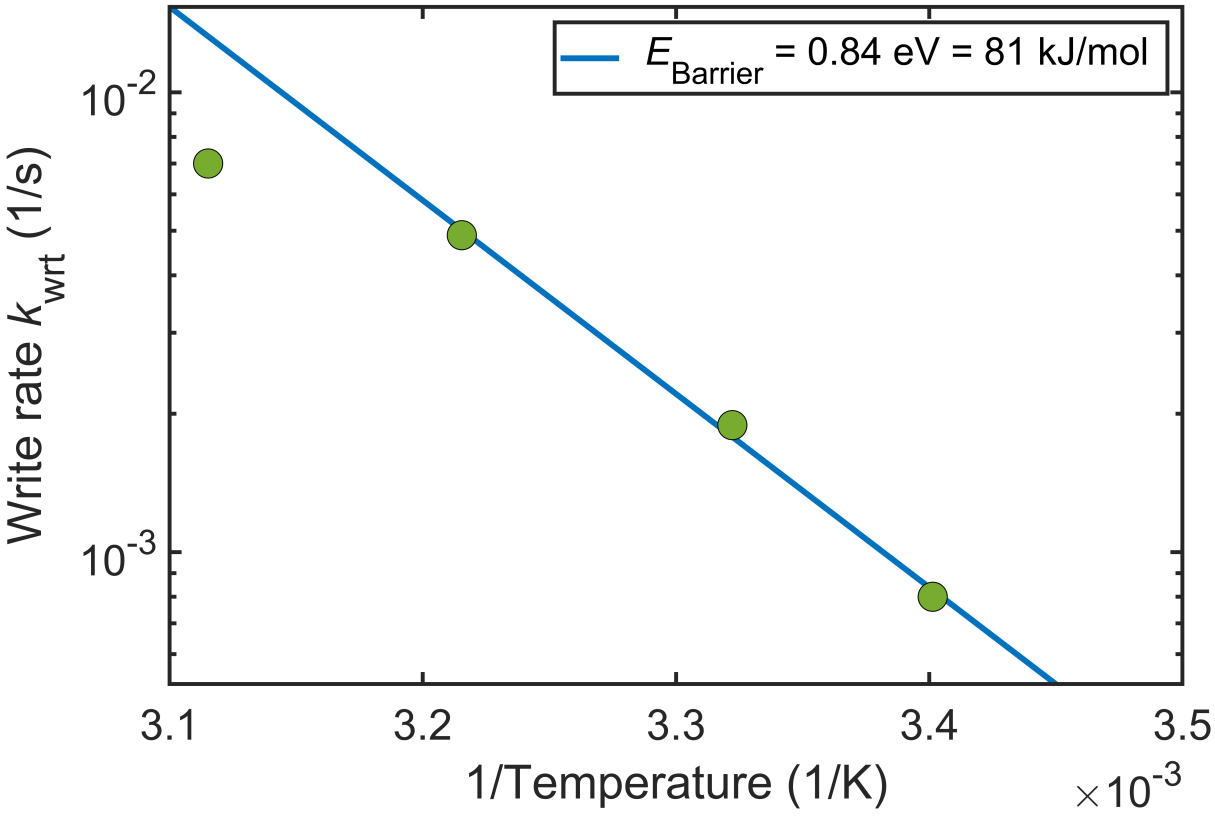

Supplementary Figure S10 Rate of DASA bleaching in a PAMS matrix as a function of temperature

The Figure shows an Arrhenius plot of the rate of bleaching (k_{wrt}) at an illumination intensity of 0.35 mW/cm^2, as a function of temperature. The data is derived from the measurement in SI Fig. 5. The energy barrier corresponding to the bleaching reaction is found to be 81 kJ/mol.

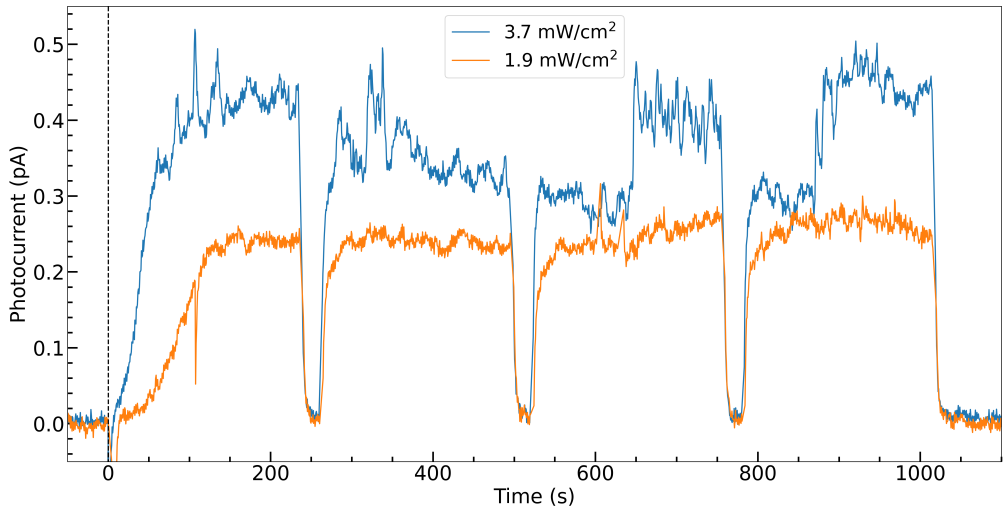

Supplementary Figure S11 Single nanowire bleaching.

This Figure shows the full single nanowire+DASA bleaching measurement result. At times $\sim 250, 500, 750$ s, the light intensity was momentarily set to the same low value as before Time = 0 s. At 1.9 mW/cm^2 (orange curve), the small exponential increase of photocurrent observed when the high-intensity illumination is turned on again, could be caused by the bleaching of the subset of DASA molecules which have back-reacted to the colored state during the low-intensity period. At 3.7 mW/cm^2 (blue curve), this bleaching should be much quicker, explaining why a near-instantaneous photocurrent increase is observed at these points of switching. As is clear from the Figure, the photocurrent at 3.7 mW/cm^2 is much less stable than at 1.9 mW/cm^2. A possible explanation of this is that trap states present in the single nanowire become more important at these elevated photocurrent levels: changes in the nanowire conductance induced by the stochastic switching on and off of trap states, will have a greater relative effect on the nanowire photocurrent when the nanowire conductance is close to its maximum.

Simulation of insect path integration

The simulation of the insect central complex (CX) consists of three main parts: the random outward path, the CX circuit that produces the memory and steering commands and the transformation of the CX output to the inward path. In what follows, we describe these three components and also how we modify the CX circuit to allow for the memory to be formed using a DASA molecular photoswitch (DASA) and nanowires.

Supplementary Text S2. Optimisation of DASA parameters. For the DASA model, we use some basic properties of the DASA (SI Text 1) to model the memory component of the above model. We next tried to fit the transmittance function in equation (1) to our data collected for the DASA (see main text). The parameters ϵ, l, ϕ and λ were known from previous measurements, and we assumed that $W_{\max} = 1.30 \times 10^{-7}\,\mathrm{J\,sec^{-1}}$ (irradiance times the area: $4.80 \times 10^{-5}\,\mathrm{J\,sec^{-1}cm^{-2}} \cdot 2.70 \times 10^{-2}\,\mathrm{cm^2}$) is a constant. The volume (V), back-reaction (k) and total concentration of the DASA (c_{tot}) were free parameters to optimise, and they were calculated by using Python and the `curve_fit` method of the SciPy library, with the only constraint that they cannot take negative values.

For the optimisation, we created a paradigm similar to the one used to collect the data for our three samples: using a spin-coated (1500 rpm) film, a thick (denoted S1 in Supplementary Fig. S11.) or thin (denoted S2 Supplementary Fig. S11.) tilted drop cast film. We exposed the modelled DASA to constant light for 7 min (S2) or 15 min (S1 and spin-coated film) and then let it recover for up to 24 h, while measuring every second. The raw data and fitted transmittance from these paradigms are summarised in Supplementary Fig. S11. The values of all the fixed parameters, our initial guess and the optimisation results are summarised in Supplementary Table S1.

Supplementary Text S3. Model of the central complex with linear memory. Our model of the CX is the same as in Stone et al. (2017)[1] , but updated to match the fly terminology and new data. The ring neurons in the insect brain encode the compass direction for a specific modality. For example, the celestial compass in the ring neurons is formed by integrating celestial cues, while the wind compass is formed by integrating information about the wind direction. The ring neurons are grouped into the two bulbs of the insect brain (left and right hemisphere), and therefore they form two bumps of activity. By using the insect heading direction (θ) we can approximate the responses of the ring neurons for a hypothetically perfect compass as

$$r_i^{\mathrm{ring}}(t) = \frac{1}{1+\mathrm{e}^{-s_i^{\mathrm{ring}}(t)}} + n_i, \qquad s_i^{\mathrm{ring}}(t) = 6.8\,\cos\Big(\theta(t) - \theta_i^{\mathrm{ring}}\Big) - 3, \tag{5}$$

were $n_i \sim \mathcal{N}(\mu = 0, \sigma = 0.1)$ is the stimuli noise and is drawn from a Gaussian distribution and $0 \leq i < 16$ ($i \in \mathbb{N}$) is the identity of each of the 16 ring neurons. The preference angle θ_i^{ring} of each ring neuron indicates the heading direction where its activity is the highest. The different compasses represented by the ring neurons in the bulbs are projected to the EPG neurons in the CX (through inhibitory connections), where they are integrated into a single compass direction. As we have only one compass, we represent the EPG activity as

$$r_i^{\mathrm{EPG}}(t) = \frac{1}{1+\mathrm{e}^{-s_i^{\mathrm{EPG}}(t)}} + n_i, \qquad s_i^{\mathrm{EPG}}(t) = -3\,r_i^{\mathrm{ring}}(t) + 0.5. \tag{6}$$

Similarly to the ring neurons, EPGs form two bumps of activity that represent the compasses formed in the two brain hemispheres. The inhibitory $\Delta 7$ neurons integrate these two bumps into one. These neurons are excited by the EPGs and also inhibited by other $\Delta 7s$ that respond to opposite heading directions. This ensures the formation of a single bump of activity and is depicted in our model as

$$r_i^{\Delta 7}(t) = \frac{1}{1+\mathrm{e}^{-s_i^{\Delta 7}(t)}} + n_i, \qquad s_i^{\Delta 7}(t) = \frac{10}{3}\,r_j^{\mathrm{EPG}}(t)\,w_{ji}^{EPG\to\Delta 7} + \frac{5}{3}\,r_k^{\Delta 7}(t-\mathrm{d}t)\,w_{ki}^{\Delta 7\to\Delta 7}, \tag{7}$$

where $w_{ji}^{EPG\to\Delta 7}$ represents the excitatory EPG to $\Delta 7$ connections and $w_{ki}^{\Delta 7\to\Delta 7}$ the inhibitory interconnections of the $\Delta 7$ layer. These connections have fixed synaptic strengths that depend on the preference angles of EPGs and Δ7s, and they are calculated as

$$w_{ji}^{EPG\to\Delta 7} = \begin{cases} 1, & \text{if } i = j \text{ or } i = j+8, \\ 0, & \text{otherwise,} \end{cases} \tag{8}$$

$$w_{ki}^{\Delta 7\to\Delta 7} = 0.5\,(\cos\big(\theta_k^{\Delta 7} - \theta_i^{\Delta 7}\big) - 1), \tag{9}$$

where θ_j^{EPG} is the preference angle of the j^{th} EPG ($0 \leq j < 16$, $j \in \mathbb{N}$), $\theta_i^{\Delta 7}$ of the i^{th} $\Delta 7$ ($0 \leq i < 8$, $i \in \mathbb{N}$), and $[*]_+ = \max(*, 0)$.

In the noduli, two types of neurons encode the egocentric speed of the animal: the LNO1 and LNO2. One LNO1 neuron responds to motion that is aligned with the front-left axis ($-\frac{\pi}{4}$) of the insect's visual field; another one to motion aligned with the front-right axis ($+\frac{\pi}{4}$). Two equivalent LNO2 neurons respond to respective backward motion. We describe the responses of these neurons in our model as

$$r_i^{\mathrm{LNO1}}(t) = [\omega_i(t)]_0^1, \qquad r_i^{\mathrm{LNO2}}(t) = [0.5 - 0.5\,\omega_i(t)]_0^1 \tag{10}$$

where $[*]_0^1 = \max(\min(*, 1), 0)$ clips $*$ between 0 and 1.

$$\omega_0(t) = v_x(t)\,\sin\Big(\theta(t) - \frac{\pi}{4}\Big) + v_y(t)\,\cos\Big(\theta(t) - \frac{\pi}{4}\Big), \tag{11}$$

$$\omega_1(t) = v_x(t)\,\sin\Big(\theta(t) + \frac{\pi}{4}\Big) + v_y(t)\,\cos\Big(\theta(t) + \frac{\pi}{4}\Big) \tag{12}$$

represent the egocentric velocity of the animal, analysed into the left ($-\frac{\pi}{4}$) and right ($+\frac{\pi}{4}$) axes from the insect's facing direction respectively. However, as the animal is assumed to always move towards its heading direction in our simulations, in every time step $\omega_0(t) = \omega_1(t) = 1/\sqrt{2}$.

In the fan-shaped body of the CX, the PFN neurons calculate the insect's allocentric velocity by combining its egocentric velocity (LNO1 and LNO2 neurons) and allocentric compass direction ($\Delta 7$ neurons) as

$$s_i^{\mathrm{PFN}}(t) = (0.5 - r_k^{\mathrm{LNO2}}(t))\,(1 - r_j^{\Delta 7}(t)) - 0.25\,r_k^{\mathrm{LNO1}}(t), \qquad (k, j) = \begin{cases} (0, i), & i < 8, \\ (1, i-8), & i \geq 8 \end{cases}, \tag{13}$$

where $0 \leq i < 16$ and $i \in \mathbb{N}$. The response of the PFN neurons is then computed as

$$r_i^{\mathrm{PFN}}(t) = \frac{1}{1 + \mathrm{e}^{-200\,s_i^{\mathrm{PFN}}(t) + 2.5}} + n_i. \tag{14}$$

If we integrate this internal representation of the insect's velocity (s_i^{PFN}) over time, we can calculate the absolute position of the insect relative to its initial position and direction as

$$c_i^{\mathrm{FC2}}(t) = c_i^{\mathrm{FC2}}(t - \mathrm{d}t) + g\,s_i^{\mathrm{PFN}}(t)\,\mathrm{d}t, \tag{15}$$

where $g = 0.025$ is the integration gain. It is possible that this integration happens internally in the FC2 neurons and it affects their responses as

$$r_i^{\mathrm{FC2}}(t) = \frac{1}{1 + \mathrm{e}^{-s_i^{\mathrm{FC2}}(t)}} + n_i, \qquad s_i^{\mathrm{FC2}}(t) = 5\,c_i^{\mathrm{FC2}}(t) - 2.5. \tag{16}$$

The tangential $h\Delta$ neurons in the fan-shaped body balance the activity between the left and right hemispheres with reciprocal connections and smoothen the activity bump. We model this as

$$r_i^{h\Delta}(t) = \frac{1}{1 + \mathrm{e}^{-s_i^{h\Delta}(t)}} + n_i, \qquad s_i^{h\Delta}(t) = -2.5 + 5\,r_j^{\mathrm{FC2}}(t) \cdot \begin{cases} 1, & 12 \leq i = j + 12, \\ 1, & 8 \leq i = j + 4 < 12, \\ 1, & 4 \leq i = j - 4 < 8, \\ 1, & i = j - 12 < 4, \\ 0, & \text{otherwise}, \end{cases} \tag{17}$$

where $0 \leq i, j < 16$ and $i, j \in \mathbb{N}$. Supplementary Fig. S12 provides a good intuition of how the above connections look like. The activity of the FC2, $h\Delta$ and $\Delta 7$ neurons contribute to the activities of the steering neurons. Essentially, the combination of the FC2 and $h\Delta$ activity at a population level provides an estimate of the goal direction and distance (starting point) in allocentric coordinates. The difference between this direction from the compass direction ($\Delta 7$) provides the egocentric direction to the starting point. This is computed by the PFL3 neurons, with a clockwise shift of the bump at the right hemisphere and a counter-clockwise shift at the left. This is modelled as

$$r_i^{\mathrm{PFL3}}(t) = \frac{1}{1 + \mathrm{e}^{-s_i^{\mathrm{PFL3}}(t)}} + n_i, \qquad s_i^{\mathrm{PFL3}}(t) = 7.5\,(0.5\,r_j^{\mathrm{FC2}}(t) - 0.5\,r_j^{h\Delta}(t) - r_k^{\Delta 7}(t)) + 1, \tag{18}$$

where $i, j, k \in \mathbb{N}$, $0 \leq i < 16$, and

$$j = \begin{cases} 7, & i = 0 \\ i-1, & 0 < i < 8 \\ i+1, & 8 \leq i < 15 \\ 8, & i = 15 \end{cases}, \qquad k = \begin{cases} i+1, & 0 \leq i < 7 \\ 0, & i = 7 \\ 7, & i = 8 \\ i-9, & 8 < i < 16 \end{cases}. \tag{19}$$

The above calculations compare the goal and heading directions in two different axes that point at 45° clockwise and counter-clockwise respectively. So, when the left visual field is aligned with the goal direction, the PFL3s in the right hemisphere will have a strong response, while those in the left will have a weaker one. This is because the compass direction becomes parallel to the represented goal direction in the right hemisphere and perpendicular to the one in the left. The opposite happens when the right visual field is aligned with the goal direction.

Finally, we summarise the activity in the left and right hemispheres independently and then take the difference between the two

$$r_{\text{motor}}(t) = \frac{1}{4}\sum_{i=0}^{7} r_i^{\text{PFL3}}(t) - \frac{1}{4}\sum_{i=8}^{15} r_i^{\text{PFL3}}(t) + n_{\text{motor}}. \tag{20}$$

The sign of the result value can be translated into a clockwise or counter-clockwise steering angle for positive or negative values respectively.

Supplementary Text S4. Use of the molecular dyes as memories in the central complex. The model described before was modified to facilitate memory formation using the properties of molecular dyes. Specifically, the incident light is modelled as proportional to the activity of the PFNs, in the form of neural activity based on the encoded allocentric velocity of equation (13),

$$I_i^{\text{FC2}}(t) = [\frac{g}{1+\mathrm{e}^{-u_i^{\text{FC2}}(t)}} + \beta]_0^1, \qquad u_i^{\text{FC2}}(t) = 2500\, r_i^{\text{PFN}}(t) - 2.5, \tag{21}$$

where $g = 0.5$. The integration now happens between the PFN and FC2 layers, by using the properties of the molecular dye and the concentration of the OFF-state molecules—equation (3). Thus, the cumulative velocity represented by the FC2 in equation (15) is replaced by the dye's transmittance,

$$c_i^{\text{FC2}}(t) = T_i(t), \tag{22}$$

as this determines the portion of light passing through the sample. The rest of the CX model was kept the same for consistency. Supplementary Fig. S13 summarises the performance of the original Stone et al.[1] model and of our variant with the molecular dyes. In our variant, we implement three versions of the memory layer, each one using the optimised parameters for a different sample.

Supplementary Text S5. Generation of a random outbound path. The outward path of the simulated insect was created using the von Mises distribution and Newtonian physics. The duration of each random path was 1000 sec and we generated a random sample every 1 sec. All the bearing directions in the path were drawn from a von Mises distribution as

$$\Delta\theta(t) \sim \text{VonMises}(\mu = 0, \kappa = 100). \tag{23}$$

Then the $\Delta\theta(t)$ was low-pass filtered to smoothen the turns of the simulated insect. Initially, $\Delta\theta(0) = 0$, while the acceleration was constant and set to $a = 0.15\,\text{m sec}^{-2}$. Also, the initial two-dimensional position of the insect was set to the centre of origin and its direction looking North as

$$x(0) = 0, \qquad y(0) = 0, \qquad \theta(0) = 0. \tag{24}$$

In each time step (t), the heading direction was updated using the pre-computed random turns as

$$\theta(t) = \theta(t - \mathrm{d}t) + \Delta\theta(t)\,\mathrm{d}t, \tag{25}$$

and this was used to calculate the two-dimensional velocity of the insect as

$$v_x(t) = v_x(t - \mathrm{d}t) + a\,\sin\theta(t)\,\mathrm{d}t, \tag{26}$$

$$v_y(t) = v_y(t - \mathrm{d}t) + a\,\cos\theta(t)\,\mathrm{d}t, \tag{27}$$

Finally, the position of the insect in the space is calculated as

$$x(t) = x(t - \mathrm{d}t) + v_x(t)\,\mathrm{d}t, \qquad y(t) = y(t - \mathrm{d}t) + v_y(t)\,\mathrm{d}t. \tag{28}$$

Supplementary Text S6. Generation of the inbound path. In every time step of the simulation, we always update our model as described above. Thus we expect that at the end of the outbound path, the path integrator of equation (15) has integrated a vector to the starting point. For the inbound path, we let equation (20) drive the steering of the insect back to the start for another 1500 sec,

$$\theta(t) = \theta(t - \mathrm{d}t) + r_{\mathrm{motor}}(t)\,\mathrm{d}t. \tag{29}$$

Now equation (15) will start integrating velocity towards the starting point, which is equivalent to removing proportions of the goal direction from the memory.

Supplementary Table S1. Parameter sets for the AP-048 dye model.

Parameter (unit)	**Spin coated 1500 rpm**	**Tilted drop cast S1** (thicker)	**Tilted drop cast S2** (thinner)	**Description**
		constant parameters		
ϵ ($M^{-1}cm^{-1}$)	1.58×10^{5}	1.58×10^{5}	1.58×10^{5}	molar absorption coefficient
l (cm)	2.50×10^{-4}	9.00×10^{-4}	3.50×10^{-4}	optical path length
ϕ (%)	0.20	0.20	0.20	quantum yield
λ (m)	6.53×10^{-7}	6.53×10^{-7}	6.53×10^{-7}	light wavelength
$W_{\max}$ ($J\,sec^{-1}$)	1.30×10^{-7}	1.30×10^{-7}	1.30×10^{-7}	maximum optical effect
		initial guess		
		before annealing		
${}^{b}k$ (sec^{-1})	6.10×10^{-5}	3.98×10^{-3}	9.60×10^{-4}	back-reaction rate coefficient
${}^{b}c_{\text{tot}}$ (M)	6.04×10^{-3}	1.18×10^{-2}	8.72×10^{-3}	total concentration of the dye
${}^{b}V$ (L)	9.74×10^{-11}	6.48×10^{-11}	1.95×10^{-11}	volume of the material
		after annealing		
${}^{a}k$ (sec^{-1})	5.80×10^{-5}	1.20×10^{-5}	1.80×10^{-5}	back-reaction rate coefficient
${}^{a}c_{\text{tot}}$ (M)	5.72×10^{-3}	1.18×10^{-2}	7.24×10^{-3}	total concentration of the dye
${}^{a}V$ (L)	3.27×10^{-10}	3.34×10^{-10}	3.01×10^{-10}	volume of the material
		optimised		
		before annealing		
${}^{b}k^{*}$ (sec^{-1})	6.28×10^{-5}	—	9.07×10^{-4}	back-reaction rate coefficient
${}^{b}c^{*}_{\text{tot}}$ (M)	6.58×10^{-3}	—	8.54×10^{-3}	total concentration of the dye
${}^{b}V^{*}$ (L)	9.60×10^{-11}	—	2.08×10^{-11}	volume of the material
		after annealing		
${}^{a}k^{*}$ (sec^{-1})	8.67×10^{-6}	8.13×10^{-6}	4.14×10^{-6}	back-reaction rate coefficient
${}^{a}c^{*}_{\text{tot}}$ (M)	6.82×10^{-3}	1.08×10^{-2}	8.27×10^{-3}	total concentration of the dye
${}^{a}V^{*}$ (L)	2.01×10^{-10}	1.85×10^{-10}	1.03×10^{-10}	volume of the material

The constant, initial guess and optimised parameters (including units) of the dye model for the different tested samples. Constant parameters (per sample) include the molar absorption coefficient, optical path length, quantum yield, wavelength of light, and maximum optical effect. The variable parameters are the back-reaction rate coefficient, total concentration of the dye, and volume of the material. These are considered different before and after annealing and were optimised separately depending on their annealed status.

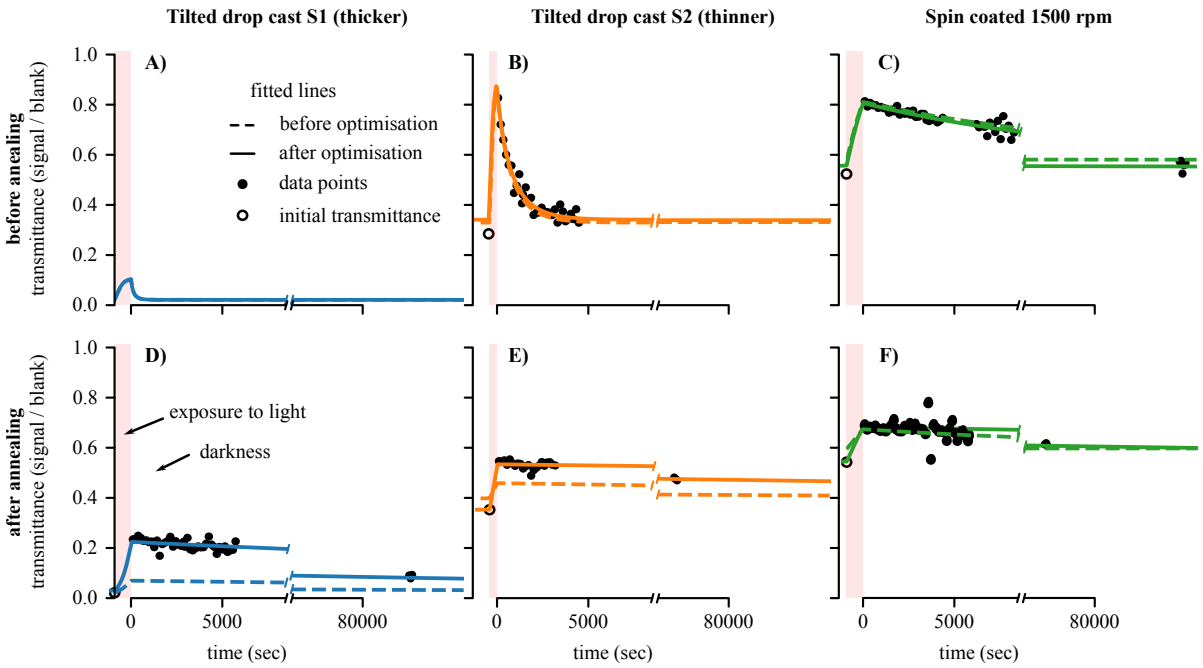

Supplementary Figure S12. Optimisation of the dye parameters based on measurements.

The parameters that model the bleaching and recovery of the dye were optimised to fit our observations (black dots). We tried three different setups for the dye: **A** and **D)** a thick (S1) or **B** and **E)** thin (S2) layer of dye on a tilted drop cast, and **C** and **F)** a thick layer on a spin-coated film (at 1500 rpm). We also tried annealing the sample (**D**, **E**, and **F**), by increasing the temperature up to 60 ° C. We first measured the transmittance before the dye was exposed to light (black empty circle). Then we exposed the sample to light (bleach) for 15 min (thick layers) or 7 min (thin layer). The red area marks the time window when the dye was exposed to light and increased its transmittance. At time 0 sec, the light is off and the recovery starts. We took measurements regularly to enhance the description of the recovery parameters. Our initial guess of the parameters is illustrated with a dashed line. Then we optimised the parameters using the measured data, resulting in the solid lines of the plots.

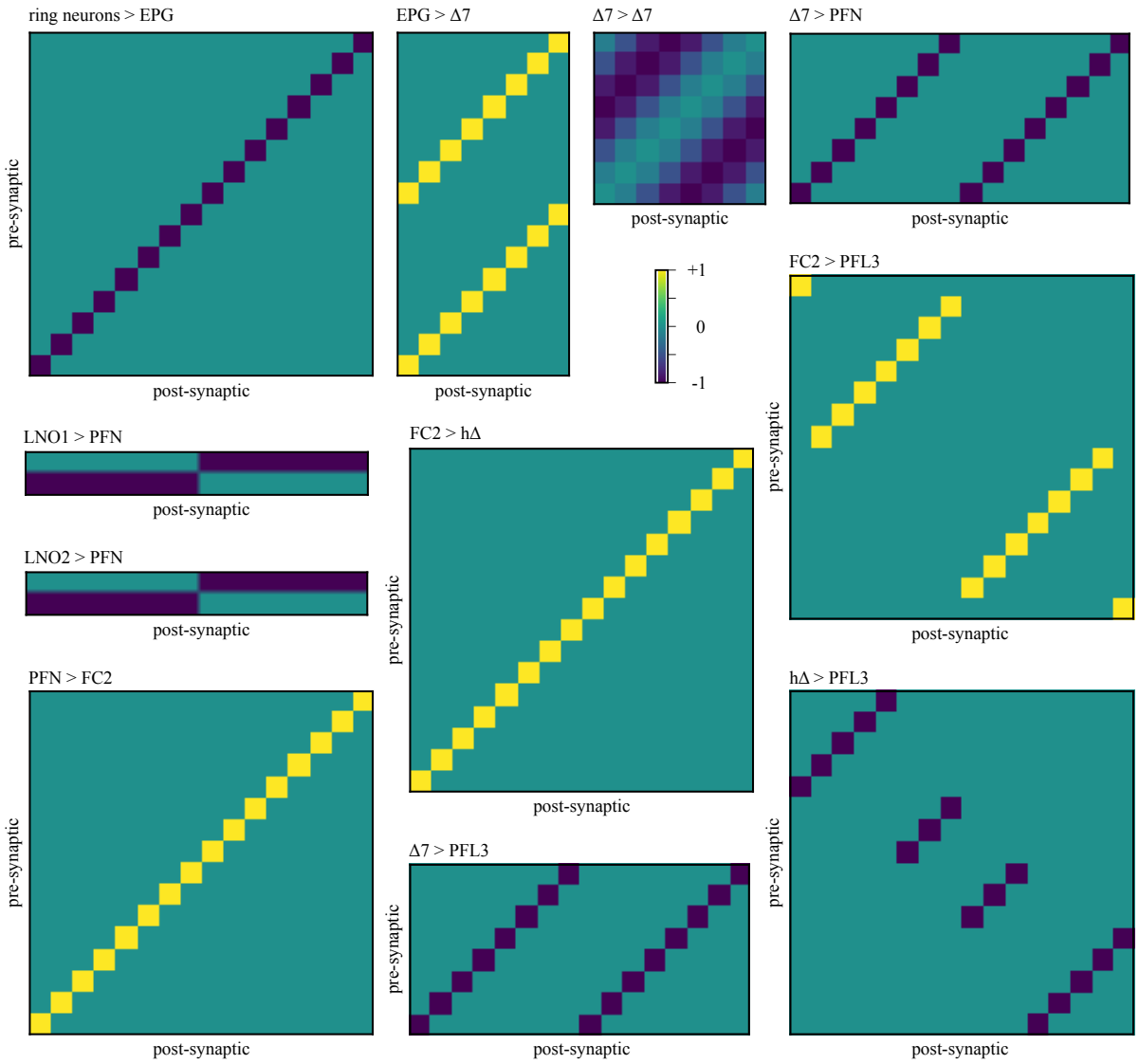

Supplementary Figure S13. Central complex circuit parameters.

The heatmaps of the figure represent the strength and sign of the model's synaptic weights. Blue represents inhibition and yellow excitation; pale green means no connection. On the vertical axis are the outputs of the pre-synaptic neurons and on the horizontal axis are the inputs to the post-synaptic ones. The indexes of neurons in both axes start from the bottom-left corner.

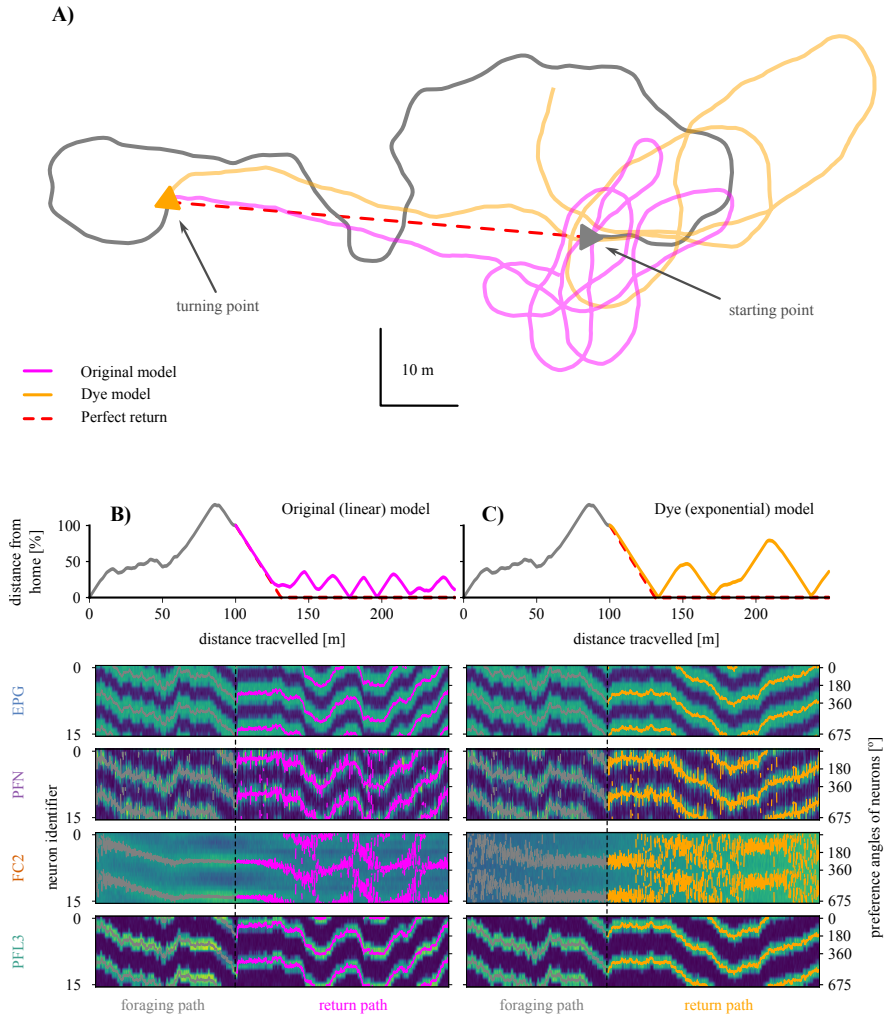

Supplementary Figure S14. Example simulation of the linear and dye models for navigation.

A) An example of an agent navigating using the birth models (random seed 2054). In grey, we show a route generated randomly for the agent, while both models integrate their paths. In magenta, we show the route of the agent when controlled using the responses of the original (linear) model. In orange, we show a similar route, generated by using the responses of the dye (exponential) model. **B)** Top: the distance from home over the distance travelled (tortuosity) for the above example when using the original model. Bottom: the responses of the neurons from the different layers of the model. On top of the responses, we plot the angle that their encoding represents based on their preference angle (the angle that they prefer to fire at). **C)** Similar plots for the dye model.

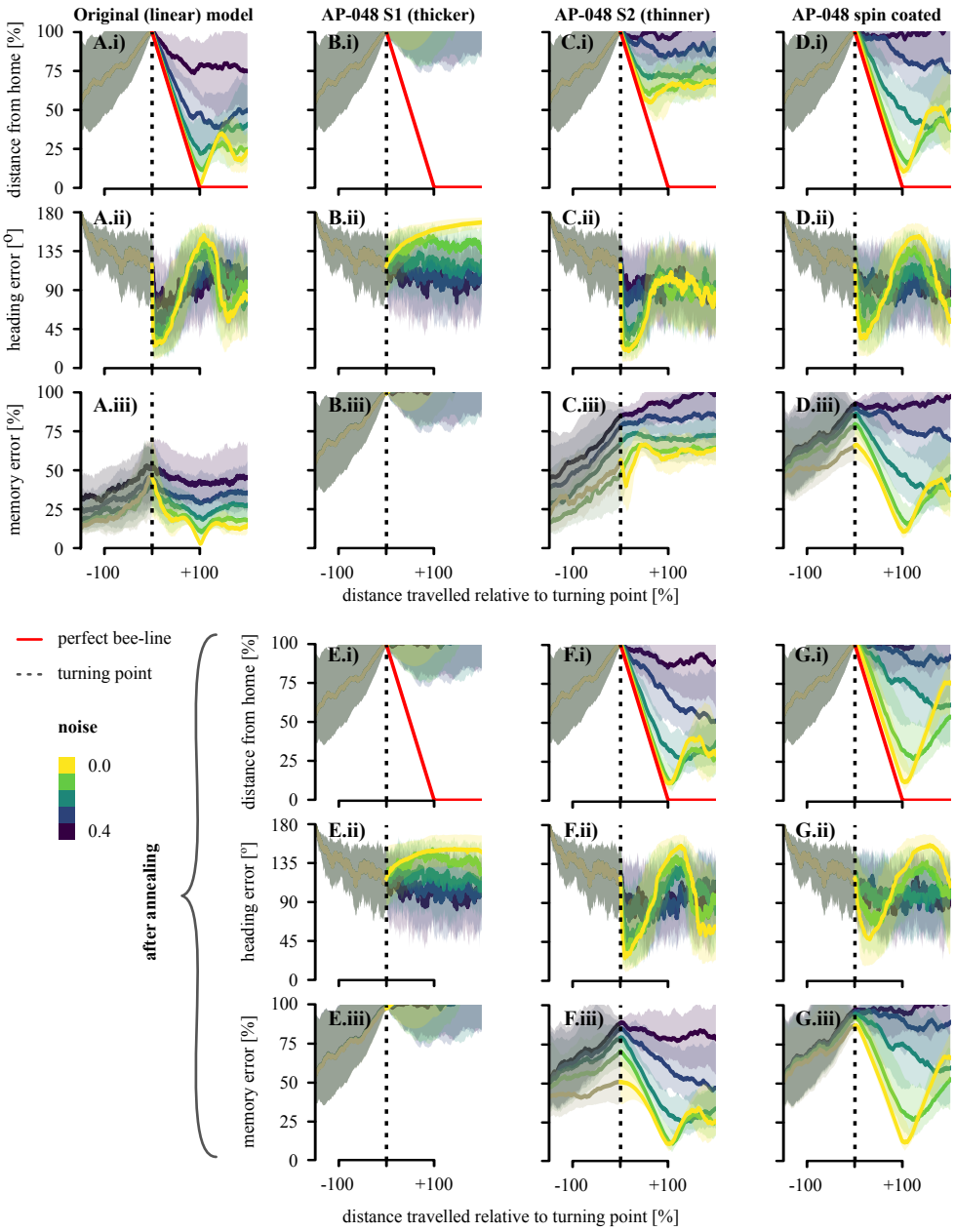

Supplementary Figure S15. Summarised simulation results for different sets of parameters and noise.

We run our navigation simulations for 100 randomly generated routes, using **A)** the original and **(B-G)** the dye model and testing all the different sets of parameters optimised for it. For each set of parameters, we plot the tortuosity of the route, the heading error of the agent, and the memory error of the agent. We also try different noise levels in the responses of the neurons, ranging from 0 % to 40 %. **i)** Tortuosity for 100 examples and both models. **ii)** Difference of the heading from the direction of the starting point. **iii)** Difference of the decoded memory vector from the starting point. The thick line shows the median; the coloured area marks the first and third quartiles.

Supplementary Text S7. Synthesis of the DASA photoswitch ("DASA 3").

S7.1. Materials and Methods Materials were obtained from commercial suppliers and used without further purification, unless otherwise noted. NMR spectra were recorded on a Bruker spectrometer at 500 MHz for ^{1}H NMR, and 125 MHz for ^{13}C NMR at 23 ° C unless otherwise stated. Chemical shifts are given in parts per million (ppm) downfield from tetramethylsilane as an internal standard, and coupling constants (J) are reported in Hertz (Hz). Splitting patterns are abbreviated as follows: singlet (s), doublet (d), triplet (t), quartet (q), septet (sept), multiplet (m), and broad (br). All ^{13}C NMR spectra are of the attached proton test (APT) variant and are phased to show nuclei coupling to an uneven number of protons as positive. High-resolution mass spectra were recorded on a Bruker SolariX ESP-MALDI-FTICR instrument equipped with a 7 Tesla magnet (the instrument was calibrated using sodium trifluoroacetate cluster ions prior to acquiring the spectra) or a MicrOTOF-QII-system using ESP (calibrated using formic acid). Analytical thin-layer chromatography was performed on Merck silica gel 60 F-254 plates. Column chromatography was performed using silica gel (45-60 µm, VWR Chemicals).

The spectroscopic studies of the DASA derivatives were carried out in toluene for solution state-studies, unless otherwise stated. For the thin film studies, the DASA derivatives were co-dissolved with poly(α-methyl)styrene (PAMS) in DCM, drop-casted on glass coverslips and allowed to dry under dark at ambient temperature. Before the studies the thin films were annealed at 50°C for 2 minutes. Steady-state absorption spectra in solution (toluene) and polymer thin films were measured by Perkin Elmer Lambda 800 UV/Vis spectrophotometer. For the kinetic measurements in thin-films, the photoswitches were pumped using a broadband halogen lamp (Schott KL2500 LCD) and the absorption changes were measured using the timedrive scan using the Lambda 800 UV/Vis spectrophotometer. The kinetics in solution state were too fast to be measured using a steady-state spectrometer. For the kinetic measurements in solutions a custom-made fast-pump probe setup was utilized. A broadband halogen lamp (Schott KL2500 LCD) was used as the pump and the absorption changes were measured simultenously using a fiber optic UV-vis setup. The fiber optic UV-vis setup consisted of a Ocean Optics DT-MINI-2-GS Deuterium Tungsten Halogen lamp as the light source, a fibreoptic variable attenuator, 4-way cuvette holder and Ocean Optics QE6500 spectrometer as the detector. The pump and the probe beams were collimated at 90° angle in the cuvette holder and the pump irradiation was controlled manually. The absorption changes were recorded using the Oceanview software from Ocean Insight.

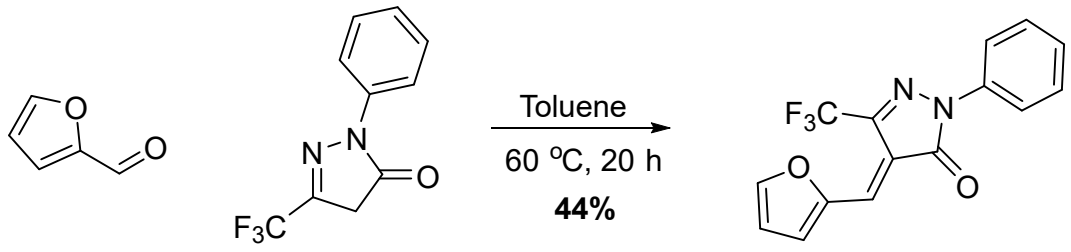

S7.2. Synthesis of FA3 The pyrazolone acceptor (0.1 g) was suspended in toluene (2 ml) at room temperature. To the mixture furfural (0.072 mL) ws added and stirred for 20 h at 60°C. As the reaction progressed, the reaction mixture turned from transparent to dark reddish-brown color to black over the period of 20 h. The completion of the reaction was monitored via TLC and the reaction was stopped after 20 hours. The heating was stopped and toluene was evaporated under vacuum. The residue was dissolved in DCM and passed through a short silica column to obtain the pure product as bright orange solid (60 mg, 44%). The purity of the compound was determined via analytical characterization and the compound was pure enough for the subsequent reactions.

^{1}H NMR (500 MHz, $CDCl_3$): δ 8.85 (d, J = 3.9 Hz, 1H), 7.88 - 7.84 (m, 2H), 7.81 (d, J = 1.7 Hz, 1H), 7.63 (s, 1H), 7.40 - 7.36 (m, 2H), 7.21 (m, 1H), 6.73 (m, 1H).^{13}C NMR (125 MHz, $CDCl_3$): δ 161.37, 150.79, 150.66, 140.09, 139.85, 137.66, 131.57, 129.00, 127.95, 126.16, 123.15, 120.99, 119.89, 119.46, 118.84, 116.67, 115.79, 115.63 HRMS (ESI): m/z calcd for $C_{15}H_{10}F_3N_2O_2$: 307.0694 [M+H]+; found: 307.0688.

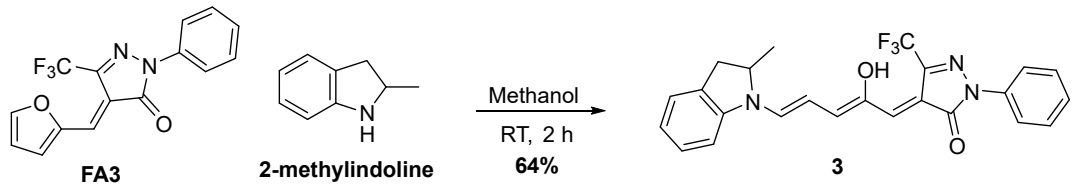

S7.3. Synthesis of DASA 3 To a stirring mixture of activated furan FA3 (0.05 g) in methanol (1.5 ml), 2-methylindoline (30 μL) was added at room temperature. Immediately after the addition of dimethylamine the reaction mixture turned from bright orange to intense greenish-blue and the reaction was stirred vigorously for 2 h at room temperature. The completion of the reaction was monitored via TLC and the reaction was stopped after 2 h stirring at room temperature. The reaction mixture was subsequently cooled to 0°C and stirred for 15 min. The solids were filtered, washed with cold methanol and dried under vacuum to get pure product as dark green solid (0.046 g, 64%).

^{1}H NMR (500 MHz, CD_2Cl_2): δ 13.19 (s, 1H), 7.97 (d, J = 7.6 Hz, 2H), 7.83 (d, J = 12.6 Hz, 1H), 7.50 – 7.43 (m, 2H), 7.37 (t, J = 7.3 Hz, 2H), 7.30 – 7.19 (m, 3H), 6.87 (d, J = 12.3 Hz, 1H), 6.61 (s, 1H), 6.50 (t, J = 12.2 Hz, 1H), 4.84 – 4.76 (m, 1H), 3.58 (dd, J = 16.2, 8.7 Hz, 1H), 2.90 (d, J = 15.6 Hz, 1H), 1.49 (d, J = 6.5 Hz, 3H). ^{13}C NMR (125 MHz, CD_2Cl_2): δ 164.69, 150.92, 147.93, 144.94, 141.17, 139.82, 139.07, 132.52, 128.83, 126.99, 126.88, 125.95, 122.58, 120.59, 111.26, 106.69, 106.53, 58.43, 36.60, 19.89. HRMS (ESI): m/z calcd for $C_{24}H_{21}F_3N_3O_2$: 440.1586 [M+H]+; found: 440.1582.

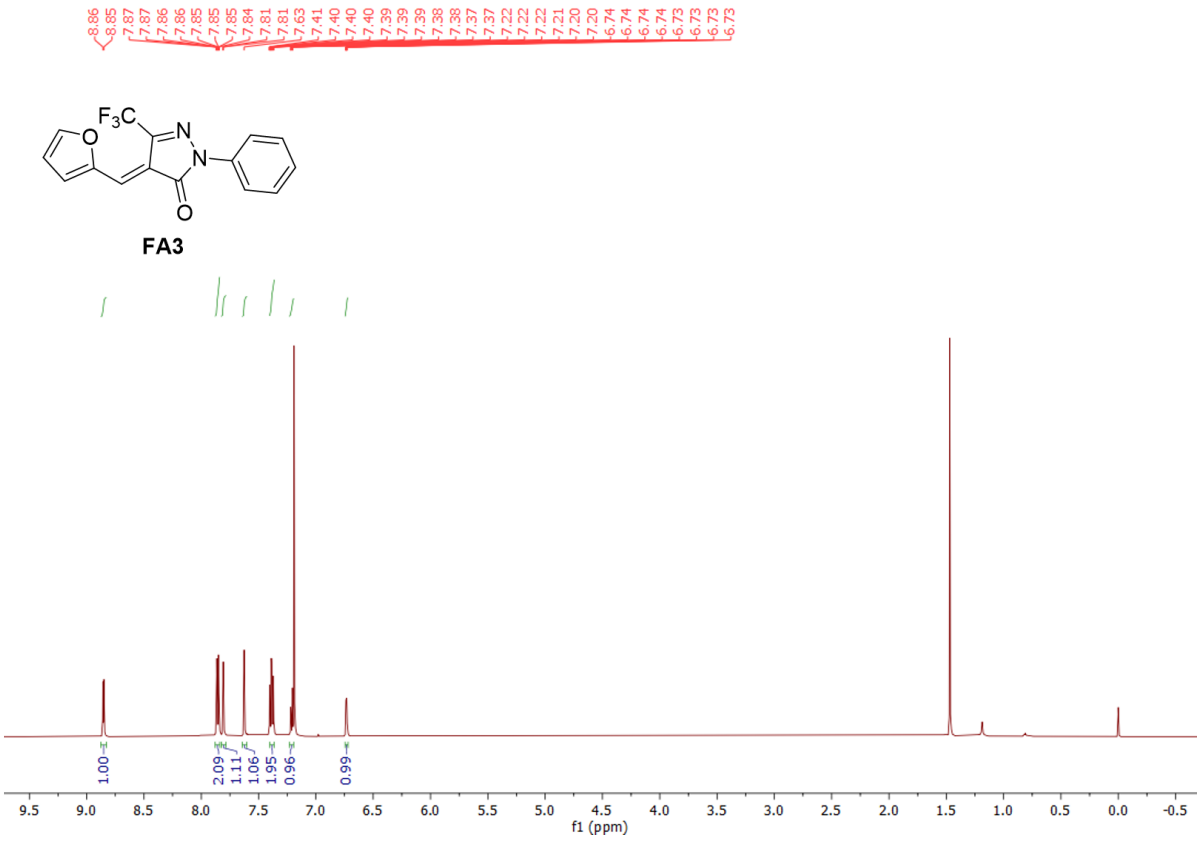

Supplementary Figure S16.1 1H NMR Spectra of FA3 in CDCl3.

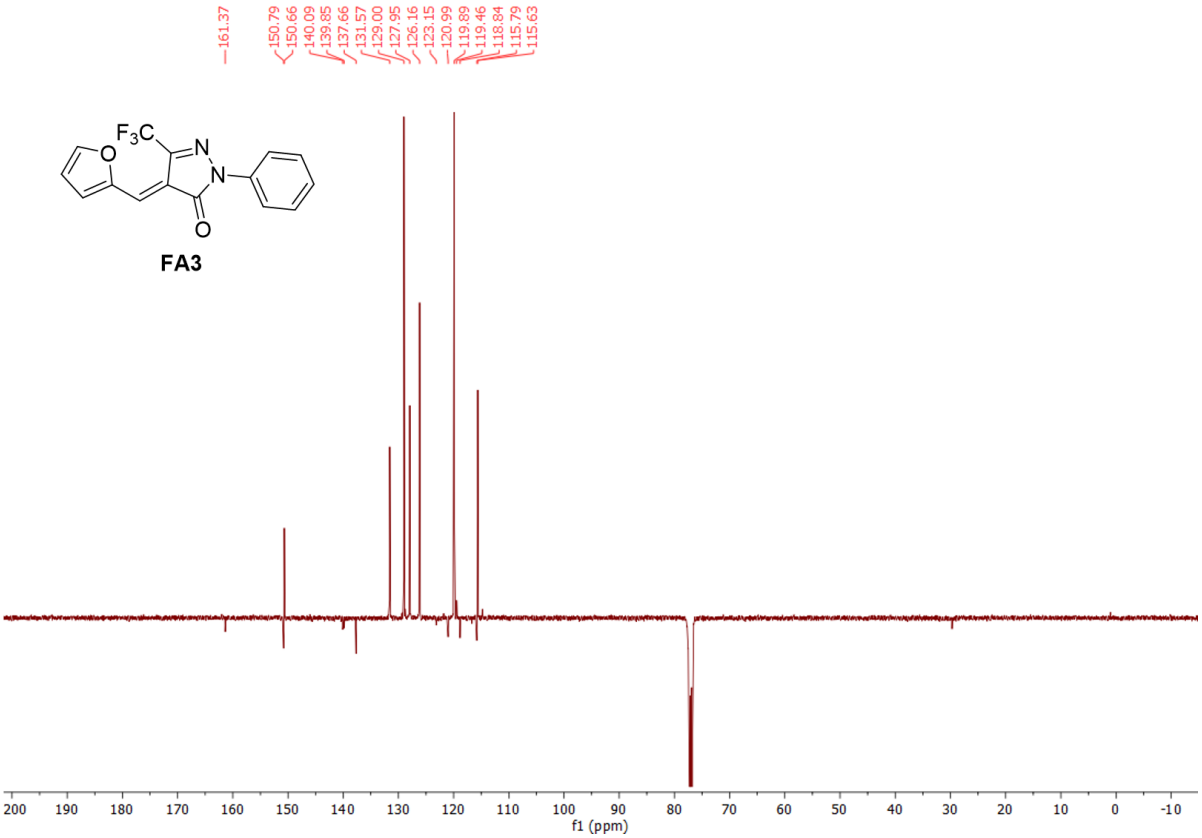

Supplementary Figure S16.2 13C APT NMR Spectra of FA3 in CDCl3.

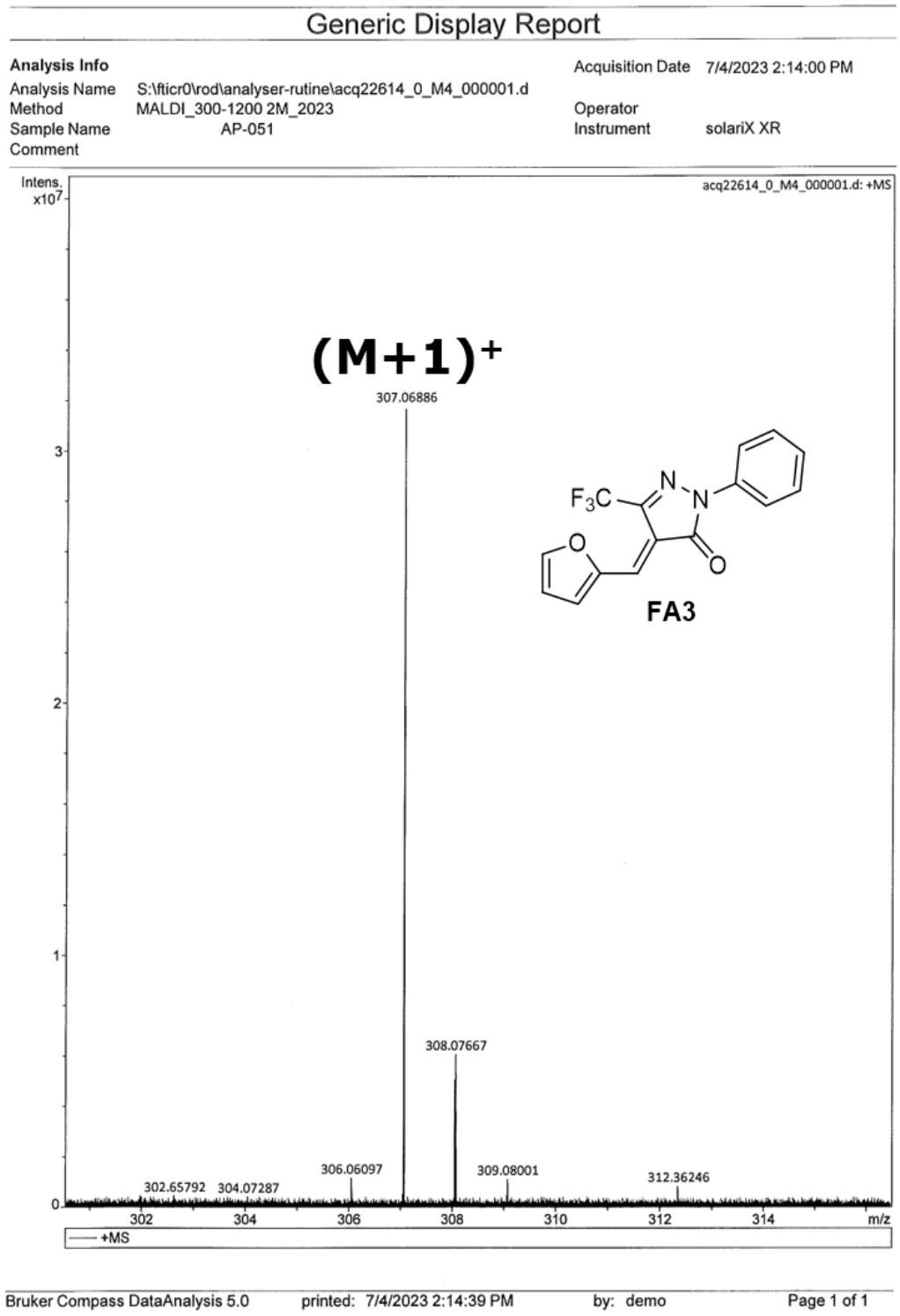

Supplementary Figure S16.3 HRMS Spectra of FA3.

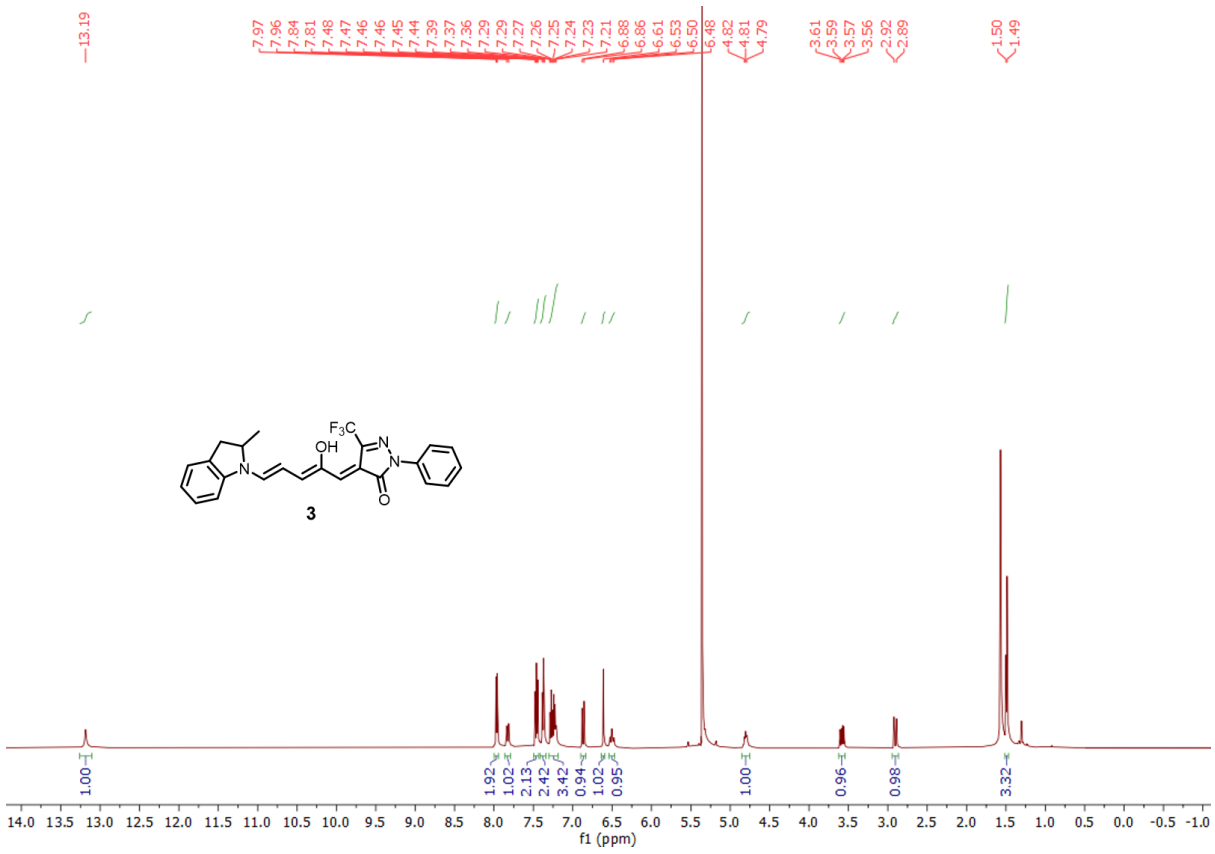

Supplementary Figure S16.4 1H NMR Spectra of DASA3 in CD2Cl2.

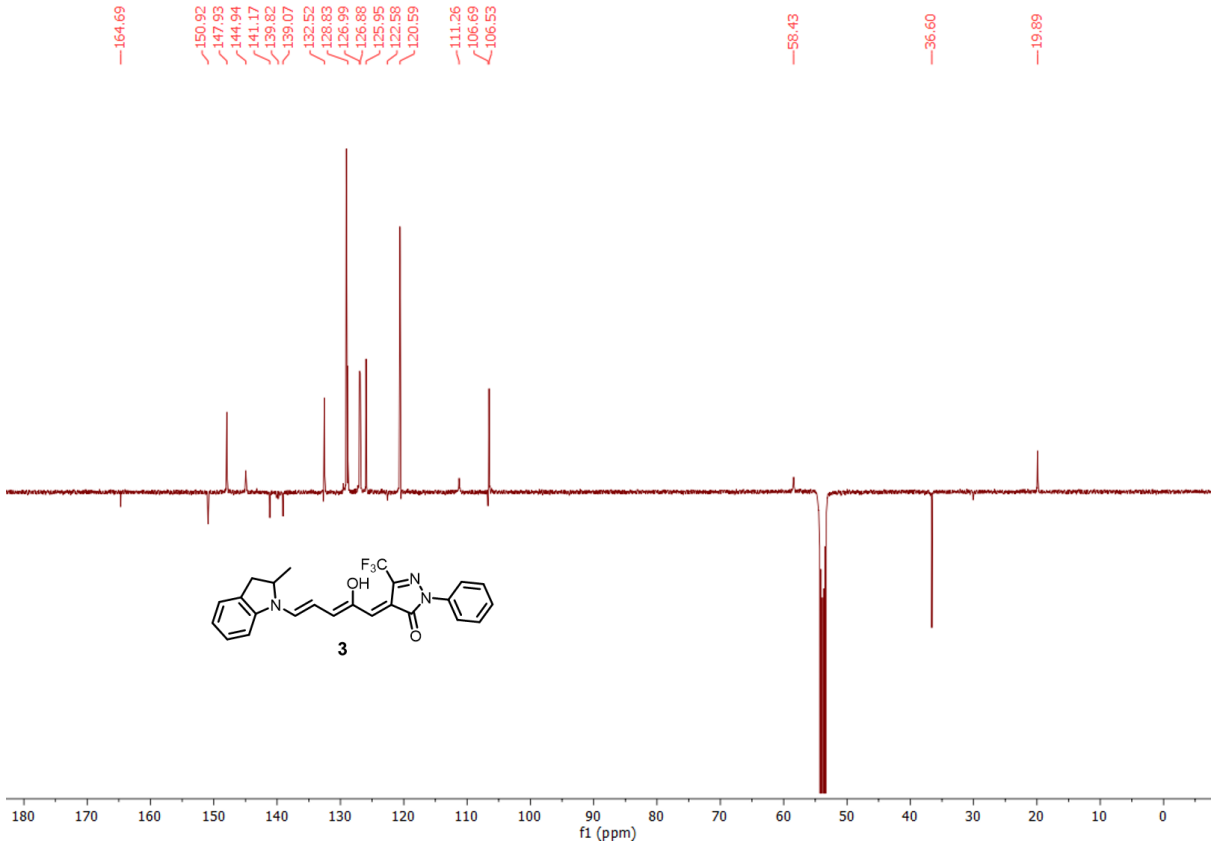

Supplementary Figure S16.5 13C APT NMR Spectra of DASA3 in CD2Cl2.

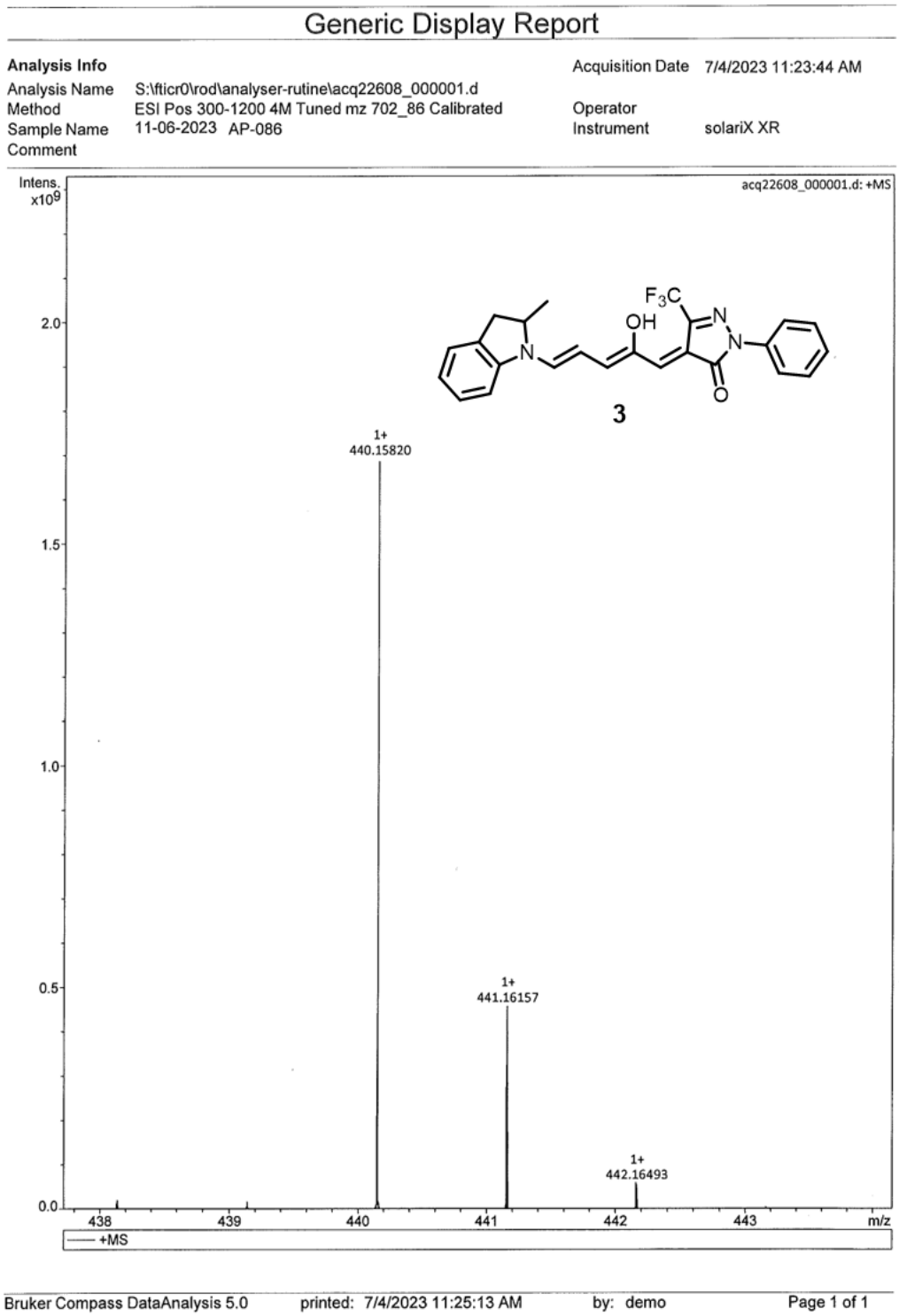

Supplementary Figure S16.6 HRMS Spectra of DASA3.

Supplementary References

[1] T. Stone, B. Webb, A. Adden, N. B. Weddig, A. Honkanen, R. Templin, W. Wcislo, L. Scimeca, E. Warrant, and S. Heinze, "An Anatomically Constrained Model for Path Integration in the Bee Brain," *Current Biology*, vol. 27, no. 20, pp. 3069–3085.e11, 2017.